

Athenaeum of Chandra Cluster Entropy Profile Tables – I. Universal Entropy Pedestals and the Bimodal Central Entropy Distribution

Kenneth W. Cavagnolo^{1,2}, Megan Donahue¹, G. Mark Voit¹, and Ming Sun¹

ABSTRACT

We present radial entropy distributions, $K(r)$, of the intracluster medium (ICM) for 199 galaxy clusters collected from the *Chandra* data archive. Radiative cooling of the ICM sets an entropy scale which is responsible for breaking the self-similarity which would otherwise be set by adiabatic hierarchical galaxy cluster formation. The entropy of the ICM can thus be used as a tool for studying the thermal history of a cluster, and as importantly, the feedback mechanisms, such as active galactic nuclei (AGN) or star formation, which naturally occur from the prodigious cooling of the ICM. We show that the entropy “pedestal” which has been observed in classic cooling flow clusters is indeed a universal feature of clusters regardless of dynamical state. We also show that the distribution of central entropy, K_0 , for our collection is consistent with models of ICM heating via AGN feedback, and that the distribution is bimodal. We suggest the observed distribution of K_0 is a reflection of AGN feedback, thermal electron conduction, and mergers. This paper focuses on the data reduction, methodology, and initial results of *ACCEPT*. We have named this project *ACCEPT* for Athenaeum of Chandra Cluster Entropy Profiles Tables. The data and results for *ACCEPT* can be found online at <http://www.pa.msu.edu/astro/MC2/accept/>.

Subject headings: I’m – a – keyword!

1. Introduction

The general process of galaxy cluster formation through hierarchical merging is well understood, but many details, such as the impact of feedback sources on the cluster environment and radiative cooling in the cluster core, are not. The nature of feedback operating

¹Michigan State University, Department of Physics and Astronomy, BPS Building, East Lansing, MI 48824

²cavagnolo@pa.msu.edu

within clusters is of great interest because of the implications for using mass-observable scaling relations in cluster cosmological studies, and for better understanding galaxy formation. The adiabatic model of hierarchical structure formation predicts clusters of galaxies which are scaled versions of each other. This model also predicts the most massive galaxies in the Universe should be rife with young stellar populations. Observations have long shown (Horner et al. 1999; Nevalainen et al. 2000; Finoguenov et al. 2001) however that clusters adhere to steeper scaling relations with larger intrinsic dispersion than theory predicts (Evrard et al. 1996; Evrard 1997). In addition, the most massive galaxies are composed of old stars (the “old, red, and dead” quandry) and have much less mass than predicted. Moreover these massive galaxies formed by $z \sim 1 - 2$ (Madau et al. 1996; Shaver et al. 1996) – the so called down-sizing problem (Cowie et al. 1996).

Because the cooling time in the cores of many clusters is much shorter than the Hubble time (Fabian 1994; Peres et al. 1998), the core region of clusters have been subject to cooling at some point in their past and most likely heating from feedback mechanisms which may initiate as a result of cooling. This secondary heating and cooling effectively decouples baryons from the dark matter and results in the breaking of self-similarity. As a consequence of radiative cooling, global cluster temperature decreases while global cluster luminosity increases. Thus, at a given mass scale, radiative cooling conspires to create dispersion in otherwise tight correlations between mass-luminosity and mass-temperature.

Additional effects of radiative cooling, such as massive cooling flows ($100-1000M_{\odot} \text{ yr}^{-1}$), have been suggested but never observed (Tamura et al. 2001; Peterson et al. 2001). Methodical searches for the end products of this gas cooling have never yielded the enormous mass sinks expected to reside in the cores of clusters (Heckman et al. 1989; McNamara et al. 1990; O’Dea et al. 1994; Voit & Donahue 1995). On the contrary, the torrents of cool gas flowing to a cluster center are more like cooling trickles (Peterson et al. 2003), depositing at most a few solar masses per year in the core and never reaching temperatures below approximately $1/3T_{\text{virial}}$. Obviously some source(s) of energetic feedback has heated the ICM to selectively remove gas with a short cooling time.

Thanks to the high-resolution optics aboard *Chandra*, previously unobserved bubbles and cavities in the ICM have been found in numerous clusters with short central cooling times. A consensus has been reached that these bubbles are blown by active galactic nuclei (AGN) and the outflow energies are sufficient to heat the ICM such that energy loss from cooling is balanced. This has made AGN the cornerstone for feedback models of ICM heating. Taken as a whole, the non-gravitational processes operating in clusters are proving to be very important for understanding how clusters form and evolve in addition to being important for understanding the formation of galaxies. These feedback processes are also interesting

because the mechanisms operating present-day in the most massive galaxies are likely also the mechanisms which were important in galaxy formation early in the Universe.

In the work presented in this paper, and Paper II, we have undertaken a ‘close to the data’ study of the ICM to better understand the physical state of gas below the cooling threshold. By studying the sub-threshold gas, we aim to gain insight to how ICM properties correlate with cluster feedback state, what can be learned of how feedback mechanisms operate, and how this feedback alters global cluster properties. To this end, we have paid particular attention to ICM entropy.

Taken individually, ICM temperature and density do not fully illuminate the cluster thermal history because they are most influenced by the underlying dark matter potential. Gas temperature reflects the depth of the potential well, while density reflects the capacity of the well to compress the gas. However, recall that at constant pressure the density of a gas is determined by its specific entropy. So using the expression for the adiabatic constant $K = P\rho^{-5/3}$, rewriting pressure and density in terms of temperature and electron density, one can define a new quantity, $K = Tn_e^{-2/3}$, where T is temperature and n_e is electron gas density, one captures the complete thermal history of the gas because only heating and cooling can change K . This quantity is typically referred to as entropy, but in actuality K is only a pseudo-entropy as relation to true thermodynamic entropy is $s = \ln K^{3/2} + \text{constant}$.

Entropy imparts the wonderfully useful property of making a gas convectively stable only when $dK/dr \geq 0$. Thus, gravitational potential wells are giant entropy sorting devices: low entropy gas sinks to the bottom of the potential well, while high entropy gas buoyantly rises to a radius of equal entropy. If a cluster were a sealed box of gravitation-only processes, then the radial entropy distribution of the ICM would strictly follow a power-law relation across all radii. Thus, any departures of the radial entropy distribution from a power-law is indicative of past heating and cooling, *i.e.* from AGN.

If feedback activity in the core of a cluster is unrelated to the gas entropy, then the expectation is that central entropy and robust indicators of feedback, *e.g.* radio-loud AGN and star formation, will be uncorrelated. But if ICM entropy and feedback are connected, then departures of $K(r)$ from a power-law can be used to better understand feedback timescales, deposition of AGN outflow energy, and ultimately the effects of feedback on cluster and massive galaxy evolution (*e.g.* truncating star formation).

In our previous work (Donahue et al. 2006, hereafter DHC06), we analyzed a sample of nine nearby ($z < 0.1$) classic cool core clusters selected for their potential to produce high-quality radial entropy profiles. In this paper, we present the results of an exhaustive study of radial entropy profiles for an archive-limited collection of observations taken from

the *Chandra* Data Archive. We have conveniently named this project *ACCEPT* which is short for Athenaeum of *Chandra* Cluster Entropy Profile Tables. For this project we cover a much broader range of L_X , T_X , and morphologies than was used in DHC06. The advantage being a uniformly analyzed collection of entropy profiles, covering a broad range of central entropies, which can then be utilized to study carefully selected sub-samples of clusters.

ACCEPT as a whole is not an unbiased, complete sample of clusters as it is drawn from the *Chandra* archive and is thus subject to selection biases. But *ACCEPT* does provide us with a powerful baseline to study any entropy-feedback connections which may exist. From our analysis we have found that the entropy pedestal observed in DHC06, and by many others previously (*e.g.* Ponman et al. 1999, Lloyd-Davies et al. 2000, Piffaretti et al. 2005), is not isolated to just cooling flow clusters, but is a feature of all clusters. We also have found two indicators of feedback – radio-loud AGN found using the NRAO VLA Sky Survey (NVSS) and star formation as evidenced by $H\alpha$ emission from the central dominant (cD) galaxy – are strongly anti-correlated with central entropy. For the first time we also note two interesting results:

1. The central entropy distribution of the full *ACCEPT* collection shows strong bimodality, while the distribution for the HIFLUGCS sub-sample shows robust multimodality.
2. There appears to exist a characteristic entropy threshold which coincides with the electron thermal conduction stability limit below which feedback proceeds and above which feedback is abated. The clusters below the limit are what would be called “active” clusters with star formation, AGN, and infrared excesses.

We defer detailed scientific discussion of the above two points, feedback timescales, and entropy scaling relations for Papers II and III of the series.

As part of this work, we have plans to make all data publicly available through two access points: 1) the NASA High Energy Space Archive (HEASARC) under the Chandra section of W3Browse¹, and 2) our own searchable, interactive database². All data tables, plots, spectra, reduced *Chandra* data products, scripts, and so on, will be available for any and all interested parties. We particularly encourage theorists to take advantage of the entropy profile library, a resource which to our knowledge is not available anywhere else as of right now.

¹<http://heasarc.gsfc.nasa.gov/W3Browse/chandra>

²<http://www.pa.msu.edu/astro/MC2/accept>

This paper focuses on the analysis methods and statistical trends of *ACCEPT*. The structure of this paper is as follows:

In §2 we outline sample-selection criteria and *Chandra* observations selected under these criteria. Data reduction is discussed in §3. Spectral extraction and analysis are discussed in §???. Our method for deriving deprojected electron density profiles is outlined in §3.2. Results and discussion of our final analysis are presented in §4. A summary this project is presented in §5. For this work we have assumed a flat Λ CDM Universe with cosmogony $\Omega_M = 0.3$, $\Omega_\Lambda = 0.7$, and $H_0 = 70 \text{ km s}^{-1} \text{ Mpc}^{-1}$. All quoted uncertainties are at the 1.6σ level (90% confidence).

2. Data Collection

Our sample was initially collected from observations publicly available in the *Chandra* X-ray Telescope’s Data Archive (CDA) as of June 2007. We first assembled a list of possible targets from multiple flux-limited surveys: *ROSAT* Brightest Cluster Sample (Ebeling et al. 1998), RBCS Extended Sample (Ebeling et al. 2000), *ROSAT* Brightest 55 Sample (Edge et al. 1990; Peres et al. 1998), *Einstein* Extended Medium Sensitivity Survey (Gioia et al. 1990), North Ecliptic Pole Survey (Henry et al. 2006), *ROSAT* Deep Cluster Survey (Rosati et al. 1995), *ROSAT* Serendipitous Survey (Vikhlinin et al. 1998), Massive Cluster Survey (Ebeling et al. 2001), and REFLEX Survey (Böhringer et al. 2004). After the first pass of data collection concluded, we continued expanding our collection by adding new archival data listed under the CDA Science Category as “clusters of galaxies” or “active galaxies”. As of submitting this paper, the result of our CDA scouring is a total of 454 observations amounting to a nominal exposure time of 15.05 Msec.

- Temperature, luminosity, and redshift ranges?

Calculation of radial entropy necessitates measurement of the radial temperature structure (discussed further in §3). To infer a temperature which is reasonably well constrained ($\pm 1.0 \text{ keV}$) we require a minimum of 2500 counts per radial bin. We also require a minimum of three radial bins for each cluster. We find the last criterion necessary to avoid isothermal temperature profiles (within the uncertainties) which are a result of under-resolving temperature structure; the consequence of which is artificially flattened entropy profiles. After applying these constraints to all the observations in our collection we are left with 262 observations for 198 clusters totaling 8.40 Msec. Table ?? lists the general properties for each cluster in *ACCEPT*.

3. Data Analysis

The purpose of undertaking the archival entropy study which resulted in *ACCEPT* was to create a library of uniformly analyzed galaxy cluster entropy profiles covering a broad range of masses, luminosities, temperatures, morphological states, and central cooling times. As presented in DHC06 and Voit et al. (2002), we have defined used the adiabatic constant, $K = P\rho^{-5/3}$, to define entropy in terms of the gas temperature, $T(r)$, and electron density, $n_e(r)$. Using these observables in place of the pressure and density yields entropy, $K(r) = T(r)n_e(r)^{-2/3}$. The following sections outline our method for deriving $K(r)$.

The radial temperature structure of each cluster was measured by fitting a single-temperature thermal model to spectra extracted from concentric annuli centered on the cluster X-ray peak. To acquire the gas density profile, we deprojected an exposure-corrected, background-subtracted, point source clean surface brightness profile (extracted in the 0.7-2.0 keV energy range) for each cluster and converted from observed surface brightness to emission density using a spatially dependent count rate conversion taken from the spectral analysis.

The temperature and deprojected density profiles were then used to derive entropy profiles. The resulting profiles were fit with two models: The first model assumes power-law only behavior while the second adds a constant central entropy, K_0 to the power-law.

Details of our reprocessing and reduction of *Chandra* data, along with discussion of our background analysis, are covered more thoroughly in DHC06 and Cavagnolo et al. 2008 (hereafter CDV08). We direct interested reader's to those papers for in-depth discussion. In this paper we simply cover the basics of deriving gas entropy from X-ray observables. The primary difference between the present analysis and that of DHC06 and CDV08, is that we have used CIAO 3.4.1 and CALDB 3.4.0 when reducing data for this project. All quoted uncertainties are 90% confidence ($\Delta\chi^2 = 2.71 = 1.6\sigma$).

3.1. Temperature Profiles

One of the two components needed to derive gas entropy is the temperature as a function of radius. We therefore constructed radial temperature profiles for each cluster in our collection. A minimum of three annuli containing 2500 counts were required to reliably constrain a temperature and detect temperature structure beyond simple isothermality. To construct the annuli for each cluster, we extracted a background-subtracted cumulative counts profile using 1 pixel width annular bins originating from the cluster surface brightness peak and extending to a radius bounded by the detector edge, or $1/2R_{180}$, whichever is smaller. Pro-

files are truncated at $1/2R_{180}$ as this is the approximate radius where temperature profiles begin to turnover (Vikhlinin et al. 2005), and we are most interested in the radial entropy behavior in the cluster core. Additionally, analysis of cluster temperature structure at large radii requires a more time consuming and customized analysis of the X-ray background as the hard-particle background has been changing rapidly since 2004.

The cumulative counts profiles were then divided into annuli containing at least 2500 counts (exact counts per annulus are listed in Table ??). For well resolved clusters, the number of counts per annulus was arbitrarily increased to reduce the resulting uncertainty of T_X and, for simplicity, to keep the number of annuli less than 50. The loss of temperature resolution from reducing the number of annuli and mixing of different gas phases in a given bin has an insignificant effect on the final entropy profiles.

Background analysis was performed using the blank-sky datasets provided in the CALDB. Backgrounds were reprocessed and reprojected to match each observation. Off-axis chips were used to normalize for variations of the hard-particle background by comparing blank-sky and observation 9.5-12 keV count rates. Soft residuals were also created and fitted for each observation to account for the spatially-varying soft Galactic background. This component was added as an additional, fixed background component during spectral fitting. Errors associated with the soft background are estimated and added in quadrature to the final error budget.

After defining annular apertures, we extracted source spectra from the target cluster and background spectra from the corresponding normalized blank-sky dataset. By standard CIAO means we created response files (ARF) and redistribution matrices (RMF) for each cluster using a flux-weighted map (WMAP) across the entire extraction region. These files quantify the effective area, quantum efficiency, and imperfect resolution of the *Chandra* instrumentation. The WMAP was calculated over the energy range 0.3-2.0 keV to weight calibration which varies as a function of position on the chip. Each spectrum was binned to contain a minimum of 25 counts per energy bin.

Spectra were fitted with XSPEC 11.3.2ag (Arnaud 1996) using an absorbed, single-temperature thermal model over the energy range 0.7-7.0 keV. Galactic absorption values, N_{HI} , are taken from Dickey & Lockman (1990). The potentially free parameters of the absorbed thermal model (WABS·MeKaL) are N_{HI} , X-ray temperature, metal abundance normalized to Solar (elemental ratios taken from Anders & Grevesse (1989)), and a normalization proportional to the integrated emission measure within the extraction region:

$$\eta = \frac{10^{-14}}{4\pi D_A^2 (1+z)^2} \int n_e n_p dV \quad (1)$$

where D_A is the angular diameter distance, z is cluster redshift, n_e and n_p are the electron

and proton densities respectively, and dV is the volume of the emission region. In all fits the metal abundance in each annulus was a free parameter and N_{HI} was fixed to the Galactic value. No systematic error is added during fitting and thus all quoted errors are statistical only.

For some clusters, more than one observation was available in the archive. We utilized the power of the combined exposure time by first extracting independent spectra, WARFs, WRMFs, normalized background spectra, and soft residuals for each observation. Then, these independent spectra were read into XSPEC simultaneously and fit with one spectral model which has all parameters, except normalization, tied among the spectra. The simultaneous fit is what is reported for these clusters, denoted by a (\dagger), in Table ??.

Results from the spectral analysis are presented in Table ?? and corresponding plots of temperature profiles are presented in the first pane of the profile gallery. Our *ACCEPT* website³ also houses plots of spectra – and their fits – for the annuli of every cluster temperature profile. As in DHC06, we find spectral deprojection does not result in significant differences between best-fit temperatures inferred for projected or deprojected quantities. Thus, for this work, we quote projected temperatures only. Deprojection of temperature should result in slightly lower temperatures in the central bins of the clusters with the steepest temperature gradients. For these clusters, the end result would be a negligible lowering of the entropy for the central-most bins. We stress that deprojection does not significantly change the shape or K_0 values we derive in this work.

3.2. Deprojected Electron Density Profiles

For predominantly free-free emission, as is the case for the cluster ICM, gas emissivity strongly depends on gas density and only weakly on temperature, $\epsilon \propto \rho^2 T^{1/2}$. Therefore the measured flux in a narrow bandpass is an excellent measure of ICM density. To reconstruct the relevant gas density as a function of physical radius we deprojected the cluster emission from high-resolution surface brightness profiles and converted to electron density using normalizations and count rates taken from the spectral analysis.

We began by extracting surface brightness profiles (second pane of the profile gallery) from the 0.7-2.0 keV energy range using concentric annular bins of size $\approx 5''$ (10 ACIS pixels) originating from the X-ray emission peak. To remove the effects of vignetting and exposure time fluctuations, we corrected each surface brightness profile by an observation

³<http://www.pa.msu.edu/astro/MC2/accept>

specific, normalized radial exposure profile. Following the recommendation in the CIAO guide for analyzing extended sources, exposure maps were created using the monoenergetic value associated with the observation count rate peak. We also tested the more sophisticated method of using spectral weights calculated for an incident spectrum with the temperature and metallicity of the observed cluster. But in the narrow band we consider, the response is relatively flat and we find no significant differences between using spectral weights or the monochromatic assumption. For all clusters the monoenergetic value used was $\sim 1.0 - 1.7$ keV.

The spectroscopic count rate and normalization in each temperature bin were then interpolated from the temperature radial grid to match the surface brightness radial grid. These interpolated values are then used to convert observed surface brightness to a deprojected electron density utilizing the deprojection technique of Kriss et al. 1983. Radial electron density can be written in terms of relevant quantities as,

$$n_e(r) = \sqrt{\frac{1.2C(r)\eta(r)4\pi[D_A(1+z)]^2}{f(r)10^{-14}}} \quad (2)$$

where 1.2 comes from the ionization ratio $n_e=1.2n_p$, $C(r)$ is the radial emission density derived using equation A1 of Kriss et al. 1983, η is the spectral normalization from Eqn. 1, D_A is angular diameter distance, z is redshift, and $f(r)$ is the 0.7-2.0 keV spectroscopic count rate. This method of density determination accounts for temperature and metallicity fluctuations which affect observed gas emissivity.

Plots of the gas density as a function of radius are presented in pane three of the profile gallery. Fundamentally, this deprojection technique requires an assumption of geometric symmetry, and while we limit ourselves to the case of spherical symmetry, we also note this assumption has little effect on our results (see Appendix A of DHC06). Errors for the gas density profile were estimated using 5000 Monte Carlo simulations of the original surface brightness profile.

Surface brightness irregularities, such as small inversions or extended flat cores, result in unstable, unphysical quantities when using the “onion” technique for deprojection. For cases where deprojection of the raw data was problematic, we resorted to fitting the surface brightness profile with the classic β -model. It is well known that the *beta*-model is only an isothermal approximation of the gas distribution and does not precisely represent all the features of the ICM (Ettori 2000; Loken et al. 2002; Hallman et al. 2007). However, we used the β -model as a means for generating a smooth analytic function which is easily deprojected. A more sophisticated method of modeling the gas density Vikhlinin et al. (2005) would avoid the problem of deprojection all together, but for our purposes here, we find such

elegant schemes unnecessary. The models used in fitting were the single and double models: of Cavaliere & Fusco-Femiano (1978):

$$S_X(r, \beta) = S_0 \left[1 + \left(\frac{r}{r_c} \right)^2 \right]^{-3\beta+0.5}$$

$$S_X(r, \beta_1, \beta_2) = S_{01} \left[1 + \left(\frac{r}{r_{c1}} \right)^2 \right]^{-3\beta_1+0.5} + S_{02} \left[1 + \left(\frac{r}{r_{c2}} \right)^2 \right]^{-3\beta_2+0.5}$$

The models were fitted using Craig Markwardt’s robust least-squares minimization IDL routines⁴. The fits were weighted using the inverse square of the surface brightness errors. Using this weighting scheme results in residuals which are near unity for, on average, the inner 80% of the radial range considered. In all cases, the β -model was an excellent fit to the data. Accuracy of errors output from the fitting routine are checked against a bootstrap Monte Carlo analysis of 1000 surface brightness realizations. Both models were considered and we established which model better represented the surface brightness profile by making a model comparison via an F-test. We considered the addition of free model components to be statistically necessary when the F-statistic was less than 0.05. A by-eye assessment was also made.

For the clusters listed in Table ??, we used the smooth analytic solution of the β -model, instead of the raw data, in deriving electron density and ultimately entropy. When necessary, the best-fit model is also plotted in pane two of the profile gallery. We emphasize that our use of a β -model fit for some clusters has not artificially introduced flattened cores into otherwise peaky surface brightness profiles. A visual comparison of the best-fit β -model and the raw surface brightness profile reinforces this point as there is little to no disagreement between the size and shape of the core region in the *beta*-models and the surface brightness.

3.3. Entropy Profiles

We derived radial entropy profiles for the clusters which comprise *ACCEPT* by taking $T(r)$ and $n_e(r)$ and calculating $K(r) = T(r)n_e(r)^{-2/3}$. To construct the radial entropy profiles, we interpolated the cluster temperature profile across the high-resolution radial grid of the deprojected electron density profile. Temperature interpolation across the central bin is applied in two ways: 1) as a linear gradient consistent with the slope of the other central bins (referred to as the ‘flat’ model) or 2) assumed to be constant across the central

⁴available at <http://cow.physics.wisc.edu/~craigm/idl/>

bin (referred to as the ‘EXTR’ model). Shown in Figure 1 is the ratio of central entropy, K_0 , derived when the central temperature, $T_{X,0}$, is assumed to be constant or interpolated. It is worth noting that both schemes yield statistically consistent values for K_0 except for the instances marked by red points.

These special cases all have steep temperature gradients in their cores with the maximum and minimum radial temperatures differing by a factor of 1.5-4.0. Extrapolating a steep temperature gradient to $r \rightarrow 0$ results in very low central temperatures ($T_X \leq 1/3 T_{\text{virial}}$) which are inconsistent with observations, most notably ?. Most importantly however, is that the flattening of entropy we observe in the cores of our sample (discussed in §4.1) is **not** a result of the method chosen for interpolating the temperature profile. For this paper we therefore focus on the results derived assuming a constant temperature across the central-most bin.

Uncertainties generated by having assumed a single-component temperature gas in each annular bin and from neglecting the effect of ICM inhomogeneity (*e.g.* cavities or bubbles) are discussed in detail in the Appendix of DHC06. Succinctly, the volume filling fraction of a second, cooler gas phase or high-entropy component must be non-trivial ($> 50\%$) in order for our entropy profiles to be significantly altered. As is discussed in DHC06, our results are robust to the presence of unresolved cool gas and mostly insensitive to X-ray surface brightness decrements.

With the exception of 24 clusters which required a β -model fit to their surface brightness profile, we have made no theoretical assumptions – besides spherical symmetry and one observationally motivated assumption for $T(r \rightarrow 0)$ – regarding the equilibrium state of the ICM, shape or depth of the underlying dark matter potential, or temperature distributions. Thus we consider these entropy profiles to be the most genuine representation of the data.

4. Results and Discussion

Each entropy profile was fit with two models, one which assumed a constant entropy pedestal (1) and another which assumed only power-law behavior (2):

$$\begin{aligned} (1) \ K(r) &= K_0 + K_{100} \left(\frac{r}{100 \text{ kpc}} \right)^\alpha \\ (2) \ K(r) &= K_{100} \left(\frac{r}{100 \text{ kpc}} \right)^\alpha. \end{aligned}$$

where K_0 is central entropy, K_{100} is a normalization for entropy at 100 kpc, and α is the power-law index. Listed in Table ?? are the results of the fitting. The table lists two sets

of values for each model: 'EXTR' which was calculated using temperature profile which was allowed to go to zero in the central bin, and 'FLAT' which was calculated using a constant temperature in the central bin. Not the entire radial range was used for fitting as the outermost bins are noisy from the “onion” deprojection scheme used. The minimum and maximum radii used during fitting are also listed. For clusters which required a double β -model fit, we restrict the fit to the innermost region as we are most interested in the entropy of the core region. The power-law index is typically much steeper for these cases, but the outer regions have power-law indices which are typical of the rest of the sample.

Shown in Figure 2 is a composite of all the entropy profiles in *ACCEPT* plotted in physical units. This figure represents the cornerstone purpose of *ACCEPT*: a uniformly analyzed collection of entropy profiles covering a broad range of central entropies. Each profile is color-coded in representation of the global cluster temperature. Overlaid on the figure is the theoretical pure cooling curve calculated by Voit et al. (2002). This curve represents the entropy profile which would result from gravitational heating alone.

In the following sections we discuss the results gleaned from analysis of *ACCEPT*. Results such as the universal entropy pedestal, the bimodal distribution of central entropy, and the asymptotic convergence of the entropy profiles to the self-similar $K(r) \propto r^{-1.1}$ power-law at $r \geq 100$ kpc.

4.1. Universal Entropy Pedestal

Arguably the most striking feature of Figure 2 is the ubiquity of a central entropy pedestal. Core flattening of surface brightness profiles (and conversely gas density) in clusters is a well established feature which led to the advent and wide usage of β -models (see §3.2). What is notable here however is that based on comparison of reduced χ^2 , none of the clusters in *ACCEPT* have an entropy distribution which is best-fit by the power-law only model. For even the most highly peaked surface brightness profiles (e.g. Abell 478, Abell 2022, Abell 2029, Abell 2129) the incredible resolving power of *Chandra* allows us to discern the subtle flattening of the gas density at small radii ($r < 10$ kpc). Only four clusters have a central entropy which is not statistically distinguishable from zero: 2PIGG 0011.5-2850, Abell 4059, MS 0116.3-0115, and MS 1008.1-1224. For these clusters it may be the case that the core region of the cluster is very small ($r_{\text{core}} \lesssim 5 - 10$ kpc) and is thus not resolved.

The departure of core entropy from the self-similar power-law behavior is a primary signature of past heating and cooling which has taken place inside the cluster during its formation. That this is a ubiquitous feature of cluster entropy profiles is telling of just how

important feedback mechanisms are to understanding the global properties of clusters and their evolution. For the whole collection, the mean of K_0 is $86.1 \pm 89.1 \text{ keV cm}^2$. Subdividing the collection into two arbitrary classes – clusters with K_0 below and above 50 keV cm^2 – we find means of $K_0 = 19.2 \pm 11.3 \text{ keV cm}^2$ and $K_0 = 155.5 \pm 80.9 \text{ keV cm}^2$, respectively. We show section §4.2 that this arbitrary cut in K_0 space is not so arbitrary, and that the low dispersion in these two subgroups of the full sample is related to the processes of AGN heating and possibly thermal electron conduction.

While one may be tempted to explain the entropy pedestal feature as a resolution effect, we direct the reader again to DHC06 where we showed using a simulated surface brightness profile for a power-law entropy distribution, that the *Chandra* PSF is not creating an envelope which limits resolution of low entropy ICM gas. Intuitively, one can see from the gallery of profiles that an entropy core of a few to tens of kpc cannot possibly arise from instrument resolution effects alone.

The PSF of course is not the only limitation on resolving ICM core entropy structure. There is the issue of our choice to use fixed angular size bins ($5''$) when extracting surface brightness profiles. This choice may introduce an artificial resolution limit which is redshift dependent. As redshift increases a fixed bin size incorporates a larger physical volume and the value of K_0 might artificially increase because each radial bin possibly contains a broader range of gas entropies. This can be understood as a type of inherited resolution bias on the central entropy. Shown in Figure 3 is a plot of K_0 versus redshift. The trend of increasing central entropy with increasing redshift seen in the figure can take on several interpretations. One interpretation is that the trend is evidence of a redshift dependant entropy lower-boundary introduced from resolution effects. Another explanation is that the number of low entropy systems is decreasing as a function of redshift.

As a test of the redshift dependence on measured central entropy, we selected all clusters with $K_0 \leq 20 \text{ keV cm}^2$ and $z \leq 0.3$ and degraded their surface brightness profiles to mimic the effect of increasing the cluster redshift. This is best illustrated using an example: consider a cluster at $z = 0.1$. For this cluster, $5'' = 9 \text{ kpc}$. Were the cluster to be moved out to $z = 0.2$, $5''$ would equal 16 kpc . To mimic moving this example cluster from $z = 0.1$ to $z = 0.2$, we can extract a new surface brightness profile using a bin size of 16 kpc instead of $5''$. This will result in a new surface brightness profile which is analogous to a cluster at a higher redshift.

This procedure of artificially redshifting clusters was used on the subsample and repeated over an evenly distributed grid of redshifts thereby creating an ensemble of degraded surface brightness profiles and hence entropy profiles. Using this degradation method we traced the relative change in central entropy as a function of redshift for each cluster with $K_0 \leq 20 \text{ keV cm}^2$ and $z \leq 0.3$. Each cluster was stepped from $z = 0.1$ to 0.38 in increments of

0.02. If the nominal redshift of the cluster was less than the next step, then that step was skipped. The effect of decreasing surface brightness due to cosmic reddening, $(1+z)^{-4}$, was also included in the degradation, however the effect of decreased signal-to-noise is not considered here.

[the work for following paragraphs is not finished to my satisfaction]:

After repeating the analysis from §?? and §?? using the degraded entropy profiles we find the effect of redshift on our central entropy measure is... ???

From our analysis of the degraded entropy profiles, we find the slope of the lower boundary in Figure 3 is steeper than it is in the degraded profiles [TRUE?]. This points to a physical mechanism as an explanation and not an observational effect. It has been suggested recently that the number of cool core clusters decreases with increasing redshift [REFS?]. We are most likely seeing this effect in our entropy profiles. If this is the case or not, we certainly find that the redshift resolution dependence is not significantly inflating the central entropy values we have measured for the clusters in *ACCEPT*[TRUE?].

4.2. Bimodality of Central Entropy and Central Cooling Time

The time required for a gas parcel to radiate away its thermal energy is a function of the gas entropy. Low entropy gas radiates profusely and is thus subject to rapid cooling and vice versa for high entropy gas. Thus, the distribution of K_0 is of particular interest because it is an indicator of the cooling timescale in the cluster core. Consequently, the K_0 distribution for a carefully selected subsample (*e.g.* HIFLUGCS or REXCESS) of *ACCEPT* can be utilized to study how, and on what timescales, feedback mechanisms operate.

In the top panel of Figure 4 is plotted the logarithmically binned distribution of K_0 . One can immediately see the distribution has at a minimum two distinct populations. In the bottom panel of Figure 4 is plotted the cumulative distribution of K_0 . If the distinct bimodality of the K_0 distribution were an artifact of binning, then one should expect the cumulative distribution to be relatively smooth. But there are clearly plateaus in the cumulative distribution, one of which coincides with the division between the two populations at $K_0 \approx 40 - 60 \text{ keV cm}^2$. To verify the presence of this bimodality we have performed two additional checks: a KMM test and examination of the central cooling time distribution.

First, we applied the KMM bimodality test of Ashman et al. (1994) to check for the presence of two statistically distinct K_0 distributions. The KMM test estimates the probability that a set of datapoints is better described by the sum of multiple Gaussians than by a single

Gaussian. We tested two cases: the first assumed that the K_0 distribution has two Gaussian components and the dispersions of these distributions are different (i.e. the heteroscedastic case). The second case was identical except with three Gaussian components. The results of the KMM test on the first case were peaks at $54.7 \pm XXX$ and $253.8 \pm YYY$ keV cm². 163 clusters were assigned to the first distribution, while 36 were assigned to the second. The KMM code also outputs a P-value, p , for each fit. Under the assumption that χ^2 describes the distribution of the likelihood ratio statistic, $1 - p$ is the confidence interval for the model used. Our bimodal KMM test returned $p = 0.000$, or 100% confidence that the bimodal distribution was a significantly better model than the single Gaussian model. We found a similar result for the second case which used three Gaussians, with peaks at 35.4 keV cm², 175.9 keV cm², and 337.5 keV cm². 140 clusters were assigned to the first distribution, 48 to the second, and 11 to the third. The p -value was again 0.000. There is little to no possibility that the K_0 distribution we observe in *ACCEPT* arises from a single Gaussian population.

As a second check, we converted entropy to cooling time and compared those values with central cooling times calculated from only the spectral results. Cooling times were calculated using the equation,

$$t_{\text{cool}} = \frac{5nkT}{2n_en_H\Lambda(T, Z)} \quad (3)$$

where t_{cool} is in seconds, n is the total ion number ($\approx 2.3n_H$ for a fully ionized plasma), n_e and n_H are the electron and proton densities respectively, $\Lambda(T, Z)$ is the cooling function at a particular temperature and metal abundance, and 5/2 is a constant appropriate for isobaric cooling. $\Lambda(T, Z)$ is calculated for each temperature bin by inputting the best-fit temperature and metal abundance into XSPEC to get a flux. The flux is then converted into Λ . The Λ values were interpolated across the radial grid of the electron density profile. Shown in Figure 5 is the logarithmically binned distribution of central cooling times.

To make a nearly one-to-one comparison, we again calculate cooling times but using the entropy as input. Assuming free-free interactions are the dominant gas cooling mechanism, entropy is related to cooling time by recasting Eqn. 5.23 in Sarazin (1986) as,

$$t_{\text{cool}} \approx 10^8 \text{ yrs} \left(\frac{K}{10 \text{ keV cm}^2} \right)^{3/2} \left(\frac{kT}{5 \text{ keV}} \right)^{-1}. \quad (4)$$

Because the central cooling times from Eqn. 3 utilize only spectroscopic information, they are mostly independent of the entropy derivation and models we fit to the data. We can thus compare the distributions of cooling time and K_0 as complementary checks for a bimodal distribution. After converting K_0 into a cooling time (bottom panel of Fig. 5) and comparing the two distributions, we find that the cooling time gaps from Eqn. 3 and Eqn. 4 are consistent with each other and occur at $t_{\text{cool}} \sim 0.7 - 1.0$ Gyrs. The bimodality of the K_0 distribution is clearly not an artifact of our analysis techniques.

A bimodal entropy distribution is expected to arise in the model of episodic AGN feedback. Voit & Donahue (2005) put forth a model of ICM heating through AGN feedback whereby outbursts of 10^{45} erg s $^{-1}$ occurring every $\approx 10^8$ yrs can maintain a quasi-steady entropy pedestal of $\approx 10 - 30$ keV cm 2 . Rare, large AGN outbursts of total energy 10^{61} erg s $^{-1}$ should push the central entropy level into the $\approx 30 - 50$ keV cm 2 range. This model predicts quite well the distribution at $K_0 \lesssim 50$ keV cm 2 , but depletion of the $40 - 60$ keV cm 2 region and populating > 60 keV cm 2 requires an additional piece of physics.

If after a cluster experiences a large AGN outburst, and the central entropy is boosted to > 30 keV cm 2 , some mechanism were to prevent the ICM from cooling, the cluster core should remain at its present entropy configuration since cooling can no longer reduce the core entropy level. Being unable to cool, these systems will never move back toward the mean of the K_0 distribution. They have been isolated beyond a hardened lower entropy limit. Subsequent mergers could continue to raise the ICM entropy until most $40 - 60$ keV cm 2 clusters are gone and nothing but > 60 keV cm 2 clusters remain. We do note however, that it is very difficult to generate enough entropy through AGN feedback and mergers alone to produce clusters with $K_0 > 300$ keV cm 2 . To make these clusters may require some form of “pre-heating” or it may be the case that these clusters were never cool.

We propose that the mechanism by which clusters in the > 30 keV cm 2 regime are stabilized against cooling is electron thermal conduction. This has been proposed before by Donahue et al. (2005) in the case of two radio-quiet galaxy clusters with $K_0 \approx 30 - 60$ keV cm 2 , and is discussed in much more detail in the forthcoming paper Voit et al. 2008. The premise of the model for conductively stabilized cluster cores is quite simply that above a critical entropy threshold, the energetic losses from radiative cooling are balanced by thermal conduction. The model relies on a “coincidence of scaling” whereby the Field length, a descriptor for the size of a gas cloud which can condense in the presence of conduction, is a function of entropy alone. It so happens that, assuming reasonable suppression, the entropy scale at which conduction balances cooling is $K_0 \approx 20 - 30$ keV cm 2 . This is rather auspicious, as it is the same entropy scale above which the K_0 distribution falls-off rapidly. In Paper II we also present the result that below this critical entropy threshold of $20 - 30$ keV cm 2 , signatures of feedback (which rely on multi-phase gas) such as star formation and radio-loud AGN are almost universally present, while above this threshold they are not.

We must mention that *ACCEPT* is not a complete, uniformly selected sample of clusters, it is simply an archive-limited analysis of publicly available *Chandra* data. As such, one may suspect that a particular type of cluster (classic cooling flows or big mergers) draw the attention of proposers and TACs alike. K_0 bimodality could be a manifestation of

40 – 60 keV cm² clusters being “boring” and thus underobserved. This possibility can be easily addressed through the study of either a complete sample of clusters or a carefully selected sample of clusters like those in REXCESS (Böhringer et al. 2007) or HIFLUGCS (Reiprich & Böhringer 2002). We stress though that this sociological explanation is highly unlikely.

4.3. Slope and Normalization of Power-law Components

Beyond ≈ 100 kpc, the entropy profiles show a striking similarity in the slope of the power-law component which is independent of the central entropy value. For the entire collection, $\alpha = 1.22 \pm 0.31$ while for clusters with $K_0 < 50$ keV cm², $\alpha = 1.22 \pm 0.26$, and for clusters with $K_0 \geq 50$ keV cm², $\alpha = 1.21 \pm 0.35$. Scaling the entropy profiles by virial temperature and virial radius does reduce the scatter in Figure 2, but we reserve detailed discussion of scaling relations for a future paper. This mean slope of $\alpha = 1.22$, is not statistically different from the theoretical value of 1.1 (Tozzi & Norman 2001) which arises from hierarchical cluster formation.

The scaling factor used in the power-law component of model-1 and model-2, K_{100} , also shows statistical similarity but with much larger dispersion. For the whole collection, the mean value of K_{100} is 131.9 ± 65.3 keV cm². Again distinguishing between clusters below and above $K_0 = 50$ keV cm², we find $K_{100} = 146.8 \pm 68.1$ keV cm² and $K_{100} = 116.4 \pm 58.7$ keV cm², respectively. Additional entropy scaling relations and their importance will be explored more thoroughly in Paper III of the *ACCEPT* series.

5. Summary and Conclusions

We have presented our analysis of 199 galaxy cluster entropy profiles derived using archival *Chandra* data, a project which we have named *ACCEPT* for Athenaeum of Chandra Cluster Entropy Profile Tables. We deprojected surface brightness profiles extracted from 5'' annuli to obtain the electron gas density as a function of radius. We also generated temperature profiles using spectra extracted from a minimum of three concentric annuli containing 2500 counts each and extending to either the chip edge or $0.5R_{180}$, whichever was smaller. Entropy profiles were then calculated from gas density and temperature using $K(r) = T(r)n(r)^{-2/3}$. Two models for the entropy distribution were then fit to each profile: power-law only and power-law plus constant entropy pedestal, K_0 .

We have demonstrated that for all clusters, the entropy profile is best described by the

model which behaves like a power-law at large radii and has a constant entropy pedestal in the core. The profiles also show a remarkable similarity at radii greater than 100 kpc, and asymptotically approach the self-similar pure-cooling curve. We have also shown that the distribution of central entropy in *ACCEPT* is at a minimum bimodal. This bimodality has a distinct peak at $\approx 20 \text{ keV cm}^2$ with a dispersion of $\approx 10 \text{ keV cm}^2$. This part of the K_0 distribution are clusters which would be dubbed “classic cooling flows” as they have central cooling times shorter than a Hubble time. The second broader peak of the distribution is at $\approx 150 \pm 80 \text{ keV cm}^2$. These clusters can be mostly classified as having disturbed morphologies or as being highly diffuse or “fluffy” with no dense, cool cores in the lot.

We propose that the observed range and distribution of central entropies in *ACCEPT* are consistent with the picture of an entropy life-cycle which at it’s heart is run by AGN feedback and conduction. Our position is strongly supported by a number of AGN feedback models and the continuing stream of literature detailing voids and bubbles in the ICM filled with radio emission associated with AGN activity. In our picture of this entropy life-cycle, clusters undergo a set of steps as follows:

1. Clusters with a central cooling time shorter than a Hubble time have been subject to prodigious core cooling at some point in their history.
2. A very small fraction of this gas condenses and flows onto the supermassive black hole in the core of the galaxy residing at the bottom of the cluster potential well.
3. Resulting AGN activity with a duty cycle of a few tens of Myrs and occurring every few hundred Myrs is capable of maintaining an entropy pedestal of $\approx 10 - 30 \text{ keV cm}^2$ as is observed in *ACCEPT*.
4. On rare occasion, an AGN outburst can supply enough energy to push the central entropy to $> 30 \text{ keV cm}^2$. However, at these entropy scales we suggest electron thermal conduction is capable of suppressing future cooling and thus setting a hard-limit above which a cluster will no longer cool.
5. After becoming conductively stable, the cluster is then subject to continual mergers which boost the gas entropy ever higher.

We suggest the above steps in a clusters entropy life-cycle describe well the observed range of central entropys and bimodality of the K_0 distribution.

There are additional consequences of this entropy life-cycle which are threshed out in Paper II. Foremost of which is that below the conductive threshold signatures of feedback which require a multiphase medium, such as AGN activity and star formation, should be

present, as where above the threshold they should be unilaterally absent. In Paper II we show that below the theoretical conduction limit of $\approx 30 \text{ keV cm}^2$, AGN activity and star formation in the central cluster galaxy, as demonstrated by radio-loud sources and $H\alpha$ emission, are universally “on” below the limit and “off” above it. We suggest this as a strong indication that the entropy life-cycle we have pieced together in this paper is most likely how feedback is regulated in clusters.

In the effort toward developing a self-regulating model of cluster feedback, we believe a better understanding of ICM entropy has proven to be pivotal. Moving forward, developers of models of massive galaxy formation, and possibly galaxy formation in general, may find the online database associated with *ACCEPT* a highly useful tool.

Kenneth Cavagnolo was supported in this work by the National Aeronautics and Space Administration through *Chandra* X-ray Observatory Archive grants AR-6016X and AR-4017A, with additional support from a start-up grant for Megan Donahue from Michigan State University. Megan Donahue and Michigan State University acknowledge support from the NASA LTSA program NNG-05GD82G. The *Chandra* X-ray Observatory Center is operated by the Smithsonian Astrophysical Observatory for and on behalf of the National Aeronautics Space Administration under contract NAS8-03060. This research has made use of software provided by the Chandra X-ray Center (CXC) in the application packages CIAO, CHIPS, and SHERPA. This research has made use of the NASA/IPAC Extragalactic Database (NED) which is operated by the Jet Propulsion Laboratory, California Institute of Technology, under contract with the National Aeronautics and Space Administration. This research has also made use of NASA’s Astrophysics Data System. Some software was obtained from the High Energy Astrophysics Science Archive Research Center (HEASARC), provided by NASA’s Goddard Space Flight Center.

REFERENCES

- Anders, E., & Grevesse, N. 1989, *Geochim. Cosmochim. Acta*, 53, 197
- Arnaud, K. A. 1996, in ASP Conf. Ser. 101: *Astronomical Data Analysis Software and Systems V*, ed. G. H. Jacoby & J. Barnes, 17–+
- Ashman, K. M., Bird, C. M., & Zepf, S. E. 1994, *AJ*, 108, 2348
- Böhringer, H., Schuecker, P., Guzzo, L., Collins, C. A., Voges, W., Cruddace, R. G., Ortiz-Gil, A., Chincarini, G., De Grandi, S., Edge, A. C., MacGillivray, H. T., Neumann, D. M., Schindler, S., & Shaver, P. 2004, *A&A*, 425, 367

- Böhringer, H., Schuecker, P., Pratt, G. W., Arnaud, M., Ponman, T. J., Croston, J. H., Borgani, S., Bower, R. G., Briel, U. G., Collins, C. A., Donahue, M., Forman, W. R., Finoguenov, A., Geller, M. J., Guzzo, L., Henry, J. P., Kneissl, R., Mohr, J. J., Matsushita, K., Mullis, C. R., Ohashi, T., Pedersen, K., Pierini, D., Quintana, H., Raychaudhury, S., Reiprich, T. H., Romer, A. K., Rosati, P., Sabirli, K., Temple, R. F., Viana, P. T. P., Vikhlinin, A., Voit, G. M., & Zhang, Y.-Y. 2007, *A&A*, 469, 363
- Cavagnolo, K. W., Donahue, M., Sun, M., & Voit, G. M. 2008, *ApJ*, 000, 0
- Cavaliere, A., & Fusco-Femiano, R. 1978, *A&A*, 70, 677
- Cowie, L. L., Songaila, A., Hu, E. M., & Cohen, J. G. 1996, *AJ*, 112, 839
- Dickey, J. M., & Lockman, F. J. 1990, *ARA&A*, 28, 215
- Donahue, M., Horner, D. J., Cavagnolo, K. W., & Voit, G. M. 2006, *ApJ*, 643, 730
- Donahue, M., Voit, G. M., O’Dea, C. P., Baum, S. A., & Sparks, W. B. 2005, *ApJ*, 630, L13
- Ebeling, H., Edge, A. C., Allen, S. W., Crawford, C. S., Fabian, A. C., & Huchra, J. P. 2000, *MNRAS*, 318, 333
- Ebeling, H., Edge, A. C., Böhringer, H., Allen, S. W., Crawford, C. S., Fabian, A. C., Voges, W., & Huchra, J. P. 1998, *MNRAS*, 301, 881
- Ebeling, H., Edge, A. C., & Henry, J. P. 2001, *ApJ*, 553, 668
- Edge, A. C., Stewart, G. C., Fabian, A. C., & Arnaud, K. A. 1990, *MNRAS*, 245, 559
- Ettori, S. 2000, *MNRAS*, 311, 313
- Evrard, A. E. 1997, *MNRAS*, 292, 289
- Evrard, A. E., Metzler, C. A., & Navarro, J. F. 1996, *ApJ*, 469, 494
- Fabian, A. C. 1994, *ARA&A*, 32, 277
- Finoguenov, A., Reiprich, T. H., & Böhringer, H. 2001, *A&A*, 368, 749
- Gioia, I. M., Maccacaro, T., Schild, R. E., Wolter, A., Stocke, J. T., Morris, S. L., & Henry, J. P. 1990, *ApJS*, 72, 567
- Hallman, E. J., Burns, J. O., Motl, P. M., & Norman, M. L. 2007, *ApJ*, 665, 911

- Heckman, T. M., Baum, S. A., van Breugel, W. J. M., & McCarthy, P. 1989, *ApJ*, 338, 48
- Henry, J. P., Mullis, C. R., Voges, W., Böhringer, H., Briel, U. G., Gioia, I. M., & Huchra, J. P. 2006, *ApJS*, 162, 304
- Horner, D. J., Mushotzky, R. F., & Scharf, C. A. 1999, *ApJ*, 520, 78
- Kriss, G. A., Cioffi, D. F., & Canizares, C. R. 1983, *ApJ*, 272, 439
- Lloyd-Davies, E. J., Ponman, T. J., & Cannon, D. B. 2000, *MNRAS*, 315, 689
- Loken, C., Norman, M. L., Nelson, E., Burns, J., Bryan, G. L., & Motl, P. 2002, *ApJ*, 579, 571
- Madau, P., Ferguson, H. C., Dickinson, M. E., Giavalisco, M., Steidel, C. C., & Fruchter, A. 1996, *MNRAS*, 283, 1388
- McNamara, B. R., O’Connell, R. W., & Bregman, J. N. 1990, *ApJ*, 360, 20
- Nevalainen, J., Markevitch, M., & Forman, W. 2000, *ApJ*, 536, 73
- O’Dea, C. P., Baum, S. A., Maloney, P. R., Tacconi, L. J., & Sparks, W. B. 1994, *ApJ*, 422, 467
- Peres, C. B., Fabian, A. C., Edge, A. C., Allen, S. W., Johnstone, R. M., & White, D. A. 1998, *MNRAS*, 298, 416
- Peterson, J. R., Kahn, S. M., Paerels, F. B. S., Kaastra, J. S., Tamura, T., Bleeker, J. A. M., Ferrigno, C., & Jernigan, J. G. 2003, *ApJ*, 590, 207
- Peterson, J. R., Paerels, F. B. S., Kaastra, J. S., Arnaud, M., Reiprich, T. H., Fabian, A. C., Mushotzky, R. F., Jernigan, J. G., & Sakelliou, I. 2001, *A&A*, 365, L104
- Piffaretti, R., Jetzer, P., Kaastra, J. S., & Tamura, T. 2005, *A&A*, 433, 101
- Ponman, T. J., Cannon, D. B., & Navarro, J. F. 1999, *Nature*, 397, 135
- Reiprich, T. H., & Böhringer, H. 2002, *ApJ*, 567, 716
- Rosati, P., della Ceca, R., Burg, R., Norman, C., & Giacconi, R. 1995, *ApJ*, 445, L11
- Sarazin, C. L. 1986, *Reviews of Modern Physics*, 58, 1
- Shaver, P. A., Wall, J. V., Kellermann, K. I., Jackson, C. A., & Hawkins, M. R. S. 1996, *Nature*, 384, 439

- Tamura, T., Kaastra, J. S., Peterson, J. R., Paerels, F. B. S., Mittaz, J. P. D., Trudolyubov, S. P., Stewart, G., Fabian, A. C., Mushotzky, R. F., Lumb, D. H., & Ikebe, Y. 2001, *A&A*, 365, L87
- Tozzi, P., & Norman, C. 2001, *ApJ*, 546, 63
- Vikhlinin, A., Markevitch, M., Murray, S. S., Jones, C., Forman, W., & Van Speybroeck, L. 2005, *ApJ*, 628, 655
- Vikhlinin, A., McNamara, B. R., Forman, W., Jones, C., Quintana, H., & Hornstrup, A. 1998, *ApJ*, 502, 558
- Voit, G. M., Bryan, G. L., Balogh, M. L., & Bower, R. G. 2002, *ApJ*, 576, 601
- Voit, G. M., & Donahue, M. 1995, *ApJ*, 452, 164
- . 2005, *ApJ*, 634, 955

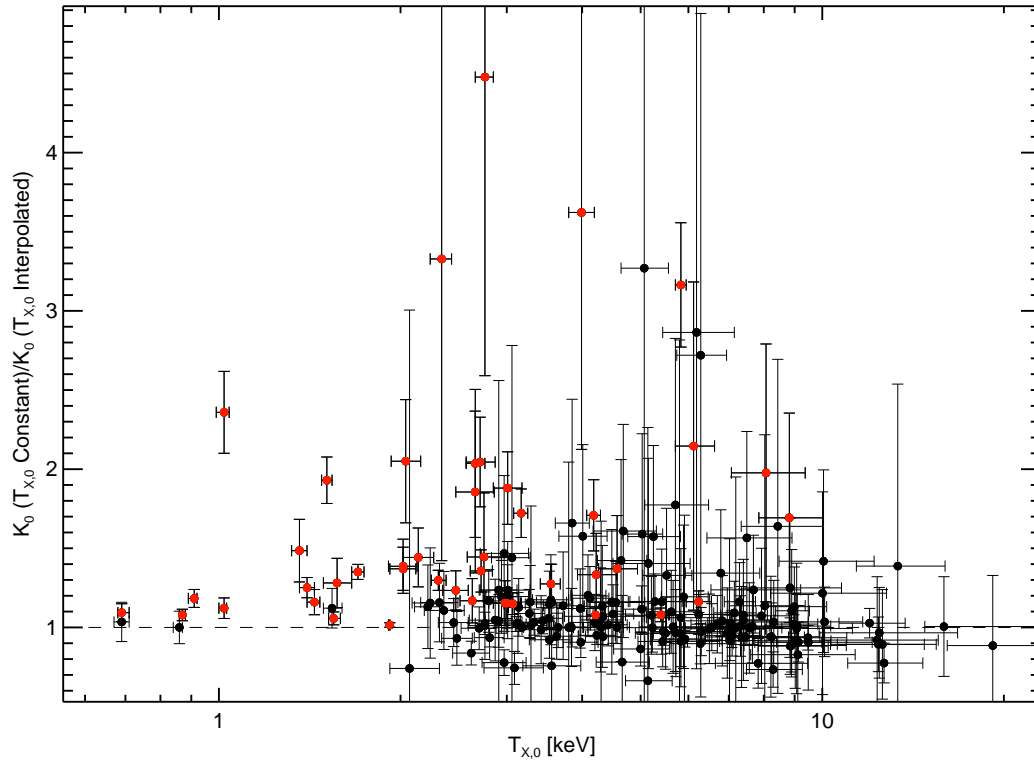


Fig. 1.— This figure shows

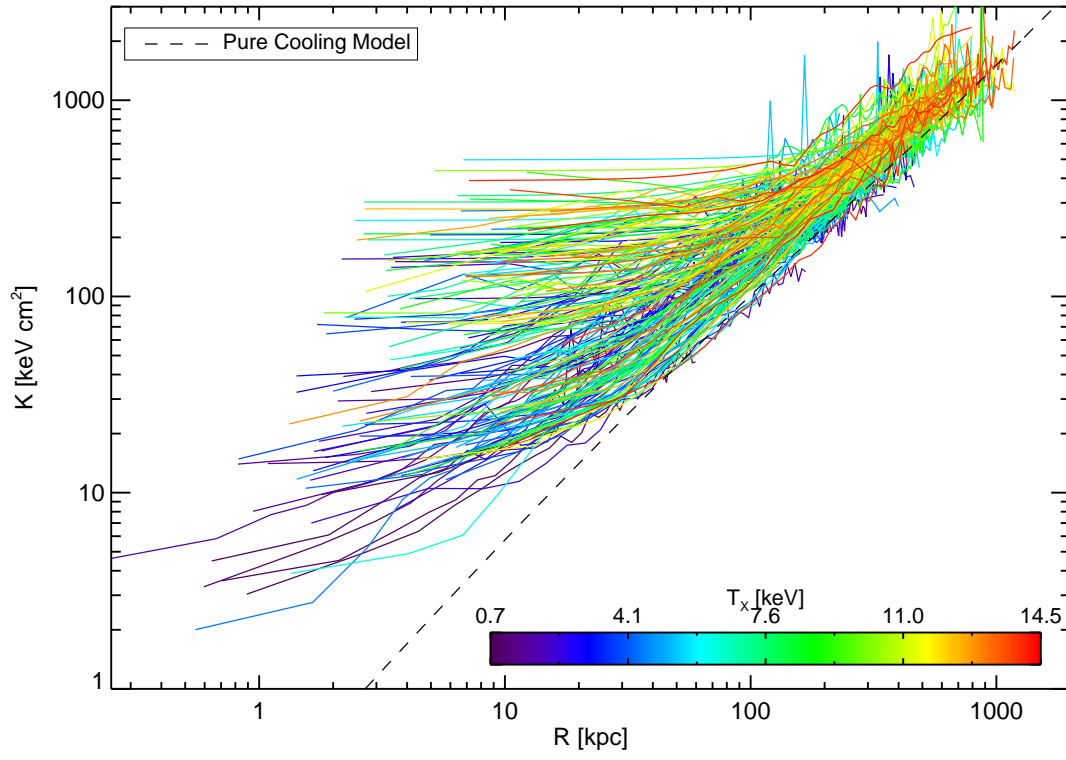


Fig. 2.— This figure shows

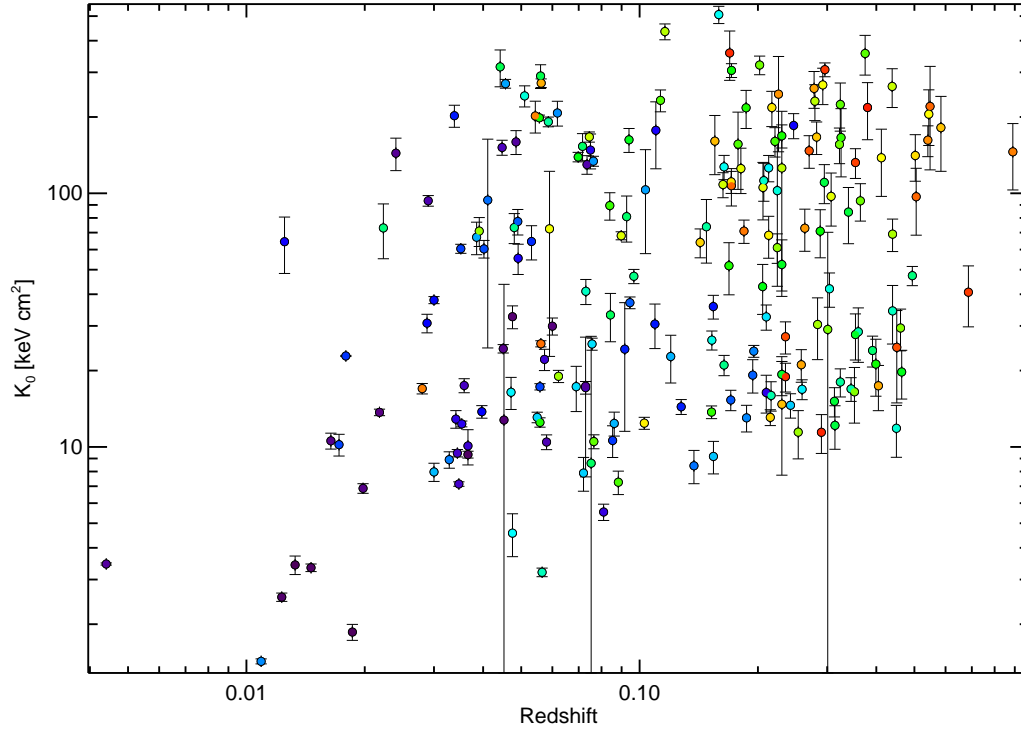


Fig. 3.— This figure shows

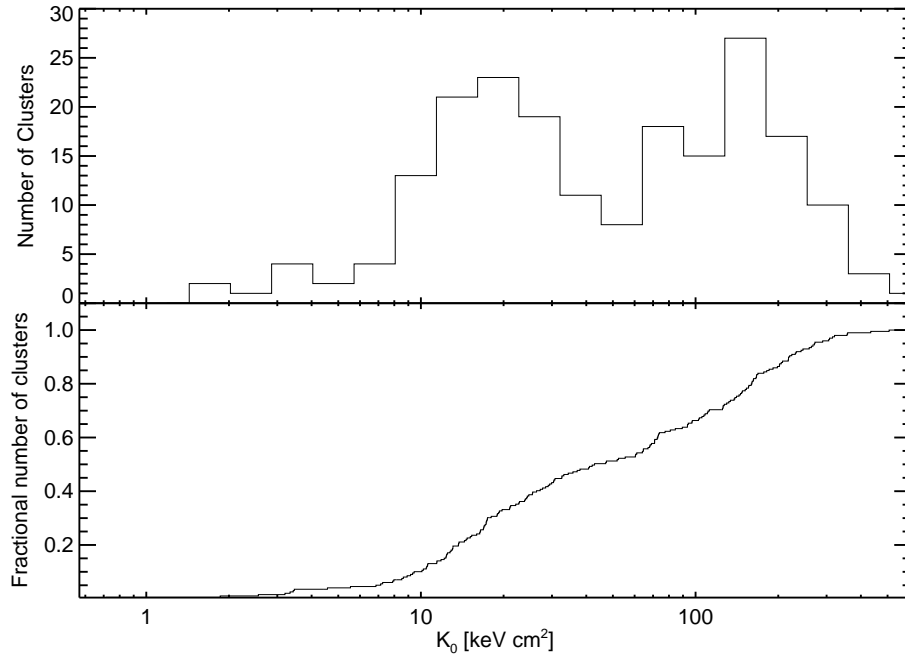


Fig. 4.— This figure shows

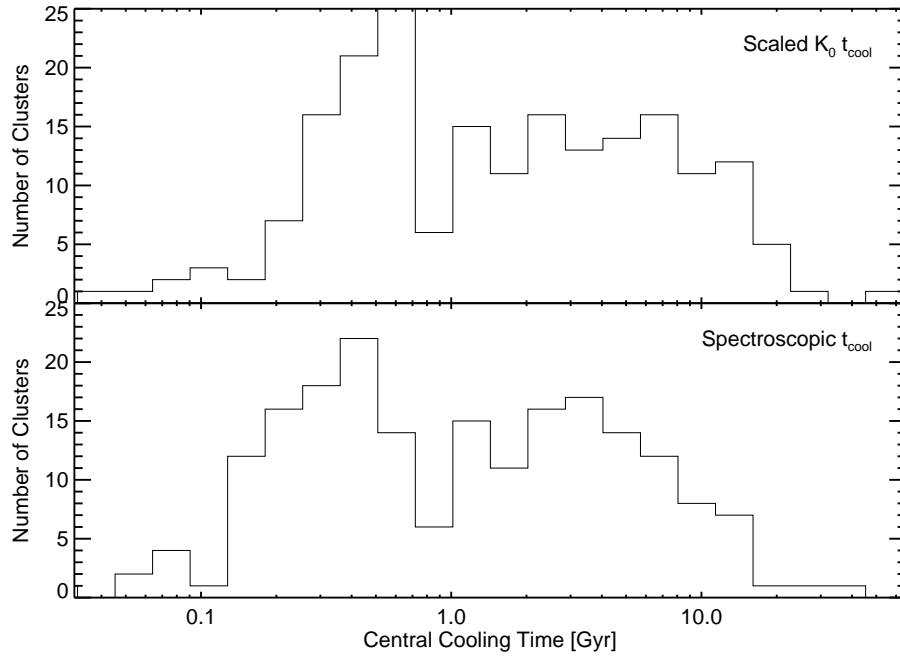


Fig. 5.— This figure shows